A nuclear signal in prophase determines centrosome positioning and ensures efficient mitotic spindle assembly

Joana T. Lima[1,2,3] and Jorge G. Ferreira[1,2]*

1 – Instituto de Investigação e Inovação em Saúde (i3S), Porto, Portugal

2 – Departamento de Biomedicina, Unidade de Biologia Experimental, Faculdade de Medicina do Porto, Portugal

3 – Programa Doutoral em Biomedicina, Faculdade de Medicina, Universidade do Porto, Portugal

* correspondence to:

Jorge G. Ferreira (ORCID: 0000-0001-6802-3696) - jferreir@ibmc.up.pt

Address: Rua Alfredo Allen, 4200-135 Porto, Portugal

Summary

Accurate centrosome separation and positioning during early mitosis relies on force-generating mechanisms regulated by a combination of extracellular, cytoplasmic, and nuclear cues. The identity of the nuclear cues involved in this process remains largely unknown. Here, we investigate how the prophase nucleus contributes to centrosome positioning during the initial stages of mitosis, by using a combination of cell micropatterning, high-resolution live-cell imaging and quantitative 3D cellular reconstruction. We show that in untransformed cells, centrosome positioning is regulated by a nuclear signal, independently of external cues. This nuclear mechanism relies on the linker of nucleoskeleton and cytoskeleton (LINC) complex that controls the loading of dynein on the nuclear envelope (NE), providing spatial cues for robust centrosome positioning on the shortest nuclear axis, prior to nuclear envelope permeabilization (NEP). Moreover, we demonstrate this mechanism is altered in cancer cells, leading to increased chromosome segregation errors. Our results demonstrate how nuclear-cytoskeletal coupling maintains a robust centrosome positioning mechanism to ensure efficient mitotic spindle assembly.

Keywords: Centrosome, prophase, nuclear envelope, LINC complex, dynein

Introduction:

Mitosis is the process by which a cell divides its genetic content into two identical daughter cells. The start of this process is typically defined as the moment when cells start to condense their chromosomes inside the nucleus[1,2]. This occurs with a near simultaneous remodelling of their cytoskeleton and a decrease in cell-matrix adhesions[3], a process regulated via integrin and cadherin signalling[4]. Cytoskeletal restructuring is a consequence of the dynamic changes that occur in the microtubule[5,6] and actomyosin networks[7,8], required to build a mitotic spindle and a stiff mitotic cortex. Subsequently, nuclear pore complexes (NPCs)[9] disassemble and the nuclear lamina depolymerizes[10], resulting in nuclear envelope permeabilization (NEP). These global changes are controlled by mitotic kinases such as PLK1 and CDK1[11–13], the latter ensuring coordination of cytoplasmic and nuclear events[12].

The goal of mitosis is to ensure the accurate segregation of chromosomes. This requires the assembly of a microtubule-based mitotic spindle that interacts with chromosomes via the kinetochores[14,15]. In human cells, the establishment of a bipolar spindle relies primarily on centrosomes[16,17], that separate along the nuclear envelope (NE) during prophase, through forces generated by motor proteins, such as kinesin-5 and dynein[18,19]. Importantly, the extent of centrosome separation and their positioning at the moment of NEP has been shown to influence mitotic fidelity[20–23], and mitotic timing[23], respectively.

Once a bipolar spindle is assembled, it must then orient inside the cell, to define a division axis. The involvement of cortical cues in mitotic spindle orientation during metaphase is well-established[24–26]. This mechanism requires the localization of the LGN-Gα1-NuMA complex to the cell cortex, which then recruits dynein to generate pulling forces on astral

microtubules. However, during the early stages of mitosis this process appears to be fundamentally different. Accordingly, we have shown that during prophase, NE-associated dynein, together with Arp2/3 activity, are required to position centrosomes in the shortest nuclear axis, independently of cortical dynein[23]. These observations suggest that a nuclear cue is required for accurate centrosome positioning prior to NEP. However, the molecular nature of this nuclear cue is still unclear.

The nucleus and some of its components have already been proposed to impact centrosome function. Accordingly, perturbations in the nuclear lamina due to loss of lamin A, leads to impaired centrosome separation and asymmetric NPC distribution in prophase[27,28]. In addition, different components of the linker of nucleoskeleton and cytoskeleton (LINC) complex, required for nucleo-cytoplasmic coupling[29], have been implicated in centrosome-nucleus tethering during cell migration, by directly associating with NE-bound dynein[28,30–32]. Moreover, the LINC complex also facilitates centrosome separation during prophase[33] and decreases chromosome scattering during prometaphase, aiding their capture after NEP[34]. Nevertheless, how these cytoplasmic and nuclear players interact during the G2/M transition to ensure accurate centrosome positioning and efficient spindle assembly remains unknown. Here, we identify the LINC complex as essential for defining the centrosome-nuclear axis during prophase in normal, near-diploid cells, by orienting centrosomes towards the shortest nuclear axis. We further show that disruption of this mechanism can lead to increased chromosome segregation errors.

Results

Chromosomally stable RPE-1 cells systematically position their centrosomes at the shortest nuclear axis

It has been previously shown that centrosome separation and positioning at the moment of NEP impacts mitotic progression and fidelity[20,22,23]. However, the degree of conservation of this mechanism between normal, untransformed cells and cancer cell lines is still unknown. To address this, we performed live-cell imaging of chromosomally stable RPE-1 cell line and two chromosomally unstable cancer cell lines of different origins (U2-OS derived from osteosarcoma and MDA-MB-468 derived from a breast adenocarcinoma), with high spatial and temporal resolution. All cell lines were seeded on micropatterned lines with a 10µm width, coated with fibronectin (FBN; Fig. 1A). This allowed us to accurately standardise cell shape and intracellular organization[23,35]. Then, we reconstructed the dynamics of centrosomes, nucleus, and cell membrane during the G2-M transition, using our previously developed tool, Trackosome[36] (Fig. S1). Detailed analysis of RPE-1 cells during the G2-M transition revealed that the long axis of the nucleus is initially aligned with the long cell axis (Fig. 1A, left panel and 1B; movie S1), likely due to a geometrical constraint imposed by the line micropattern, as was previously shown for interphase cells[37]. Once cells start to round up in preparation for mitosis, as measured by the decrease in cell membrane eccentricity, the long nuclear axis progressively diverges from the long cell axis (Fig. 1B), suggesting that mitotic cell rounding uncouples the two parameters. This reorientation occurs simultaneously with the movement of centrosomes to opposite sides of the nucleus (Fig 1C; green box). Consequently, at NEP, centrosomes are positioned on the shortest nuclear axis (Fig. 1C, 1D). Importantly, this behaviour is not observed in the two cancer cell lines. In U2-OS

cells, mitotic cell rounding is altered in comparison with RPE-1 cells (Fig. 1A, middle panel; 1B, 1E; ****$p<0.001$) and the nucleus maintains alignment with the main cell axis almost until the moment of NEP (Fig. 1E; movie S2; ****$p<0.001$). As a result of this physical constraint, centrosomes separate, but fail to position on the shortest nuclear axis at NEP (Fig. 1F, 1G; *$p= 0.0227$). On the other hand, MDA-MB-468 cells are morphologically distinct from RPE-1 or U2-OS. They are rounder and have a smaller area of adhesion to the micropatterned substrate (Fig. 1A, right panel; movie S3). As a result, they do not exhibit the decrease in cell membrane eccentricity normally observed during mitotic cell rounding (Fig. 1B, 1H; ****$p<0.001$). Consequently, the long nuclear axis is randomly oriented inside the cell (Fig. 1H). In addition, centrosomes in MDA-MB-468 often show incomplete separation and are unable to reach opposite sides of the nucleus at NEP (Fig. 1I; ****$p<0.001$). This defect in centrosome separation could be due to the decrease in cell adhesion, which affects the activity of kinesin-5[23], essential for the initial stages of centrosome separation. Consequently, centrosomes are randomly positioned relative to the nucleus at the moment of NEP (Fig. 1J; **$p<0.026$). Overall, our data show that RPE-1 cells have a robust centrosome positioning mechanism during the G2-M transition, and this mechanism is compromised in cancer cells.

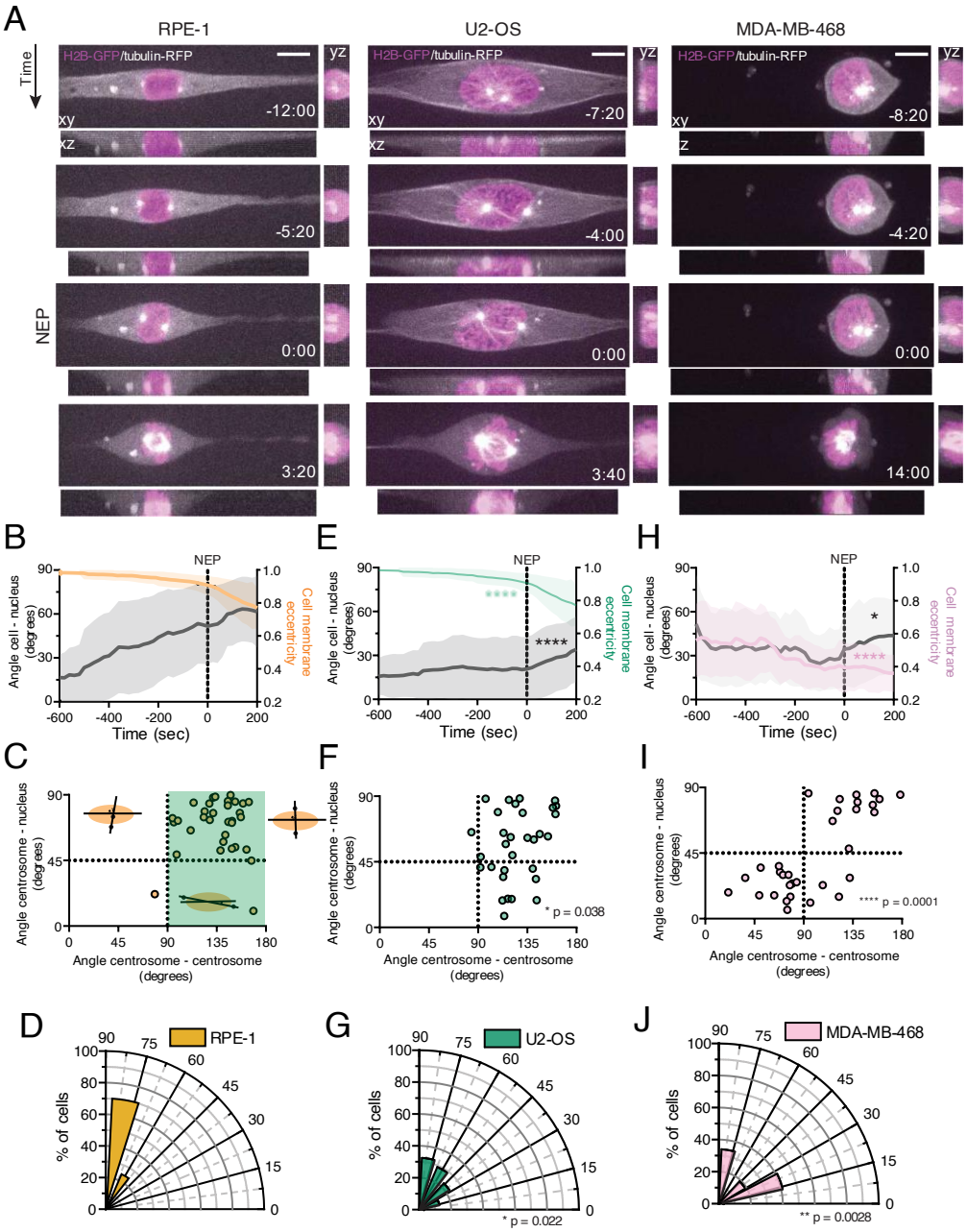

Figure 1 – Chromosomally stable, near-diploid cells efficiently separate and position their centrosomes at the shortest nuclear axis

(A) Representative frames from a movie of a near-diploid, untransformed RPE-1 cell (left panel) and chromosomally unstable U2-OS (middle panel) and MDA-MB-486 (right panel) cancer cells, stably expressing H2B-GFP and RFP-tubulin, seeded on a 10µm wide-micropatterned line, showing centrosome movement and the overall cellular reorganisation in preparation for mitotic entry. Time is in min:sec and time zero corresponds to NEP. Scale bar = 10µm. **(B)** Quantification of cell membrane eccentricity (orange) and the angle between the longest cell axis and longest

nuclear axis (Angle cell-nucleus; gray), of RPE-1 cells during mitotic entry, obtained with our custom-made MATLAB script (see also Fig. S1). Line represents mean value and shaded area corresponds to SD (n=33). Dashed line represents the moment of NEP. **(C)** Correlation between centrosome separation to opposite sides of the nucleus (angle centrosome-centrosome; x axis) and centrosome positioning relative to the shortest nuclear axis (angle centrosome-nucleus; y axis), at the moment of NEP for RPE-1 cells. Cells that efficiently separate their centrosomes will present high values of centrosome-centrosome angle, and therefore locate at the right half of the graph. Cells that correctly position their centrosomes at the shortest nuclear axis will cluster at the upper half of the graph. **(D)** Polar plot quantifying centrosome positioning relative to the shortest nuclear axis at NEP for RPE-1 cells. **(E)** Quantification of cell membrane eccentricity (green; ****p<0.001) and angle between the longest cell axis and longest nuclear axis (angle cell-nucleus; gray; ****p<0.0001) during mitotic entry for U2-OS cells. Line represents mean value and shaded area corresponds to SD (n=31). Dashed line represents moment of NEP. **(F)** Correlation between centrosome separation to opposite sides of the nucleus (angle centrosome-centrosome; x axis; *p=0.036) and centrosome positioning relative to the shortest nuclear axis (angle centrosome-nucleus; y axis), at the moment of NEP, for U2-OS cells. **(G)** Polar plot quantifying centrosome positioning relative to the longest nuclear axis at NEP for U2-OS cells (*p= 0.022). **(H)** Quantifications of cell membrane eccentricity (pink; ****p<0.0001) and angle between the longest cell axis and longest nuclear axis (angle cell-nucleus; gray; * p=0.011), of MDA-MB-468 cells during mitotic entry. Line represents mean value and shaded area corresponds to SD (n=32). Dashed line represents moment of NEP. **(I)** Correlation between centrosome separation to opposite sides of the nucleus (angle centrosome-centrosome; x axis; ****p<0.001) and centrosome positioning relative to the shortest nuclear axis (angle centrosome-nucleus; y axis), at the moment of NEP for MDA-MB-468 cells. **(J)** Polar plot quantifying centrosome positioning relative to the longest nuclear axis at NEP for these MDA-MB-468 cells (**p=0.028).

Mitotic cell rounding is not the major determinant for centrosome positioning

Given that cancer cells failed to correctly position centrosomes on the shortest nuclear axis and displayed altered mitotic cell rounding, we wondered if the two events were interconnected. This is particularly relevant since it was previously shown that mitotic rounding is essential for providing the necessary space to assemble a mitotic spindle [23,39–41]. To test this hypothesis, we proceeded to interfere with mitotic cell rounding in RPE-1

cells, by either impairing it or accelerating it. Mitotic rounding requires both cortical retraction and adhesion disassembly. Therefore, we started by acutely treating cells with a Rho-associated protein kinase (ROCK) inhibitor (Y-27632; Fig. 2A, B), known to decrease actomyosin contractility and delay cortical retraction[8]. Upon treatment with Y27632, centrosomes were still able to separate and position correctly on the shortest nuclear axis (Fig. 2C-F), although the rate of cell rounding was delayed due to an impairment of cortical retraction (Fig. 2G, ***$p<0.001$). This is in agreement with our previous observations in HeLa cells[23]. Next, we proceeded to interfere with adhesion disassembly by expressing a mutant form of Rap1 (Rap1Q63E; Rap1*), that effectively blocks mitotic rounding[3] (Fig. 2H-J, ***$p<0.001$). Delaying adhesion disassembly in RPE-1 cells did not affect centrosome separation or positioning on the shortest nuclear axis (Figure 2M, 2O; n.s. – not significant). These results indicate that delaying cell rounding in RPE-1 cells does not impact centrosome positioning at NEP. Next, we tested the effect of inducing premature rounding by treating cells with Calyculin-A (CalA), a protein phosphatase inhibitor that increases the phosphorylation of Ezrin/Radixin/Moesin (ERM) proteins and triggers cell rounding in adherent cells[42]. Acute treatment with CalA led to a faster rounding of the cells (Fig. 2O. P; ***$p<0.001$), as anticipated. Nevertheless, this did not significantly affect centrosome separation or positioning at NEP (Fig. 2Q, R; n.s. – not significant). Overall, we conclude that centrosome positioning in RPE-1 cells during early mitosis is a robust process, that occurs independently of mitotic cell rounding.

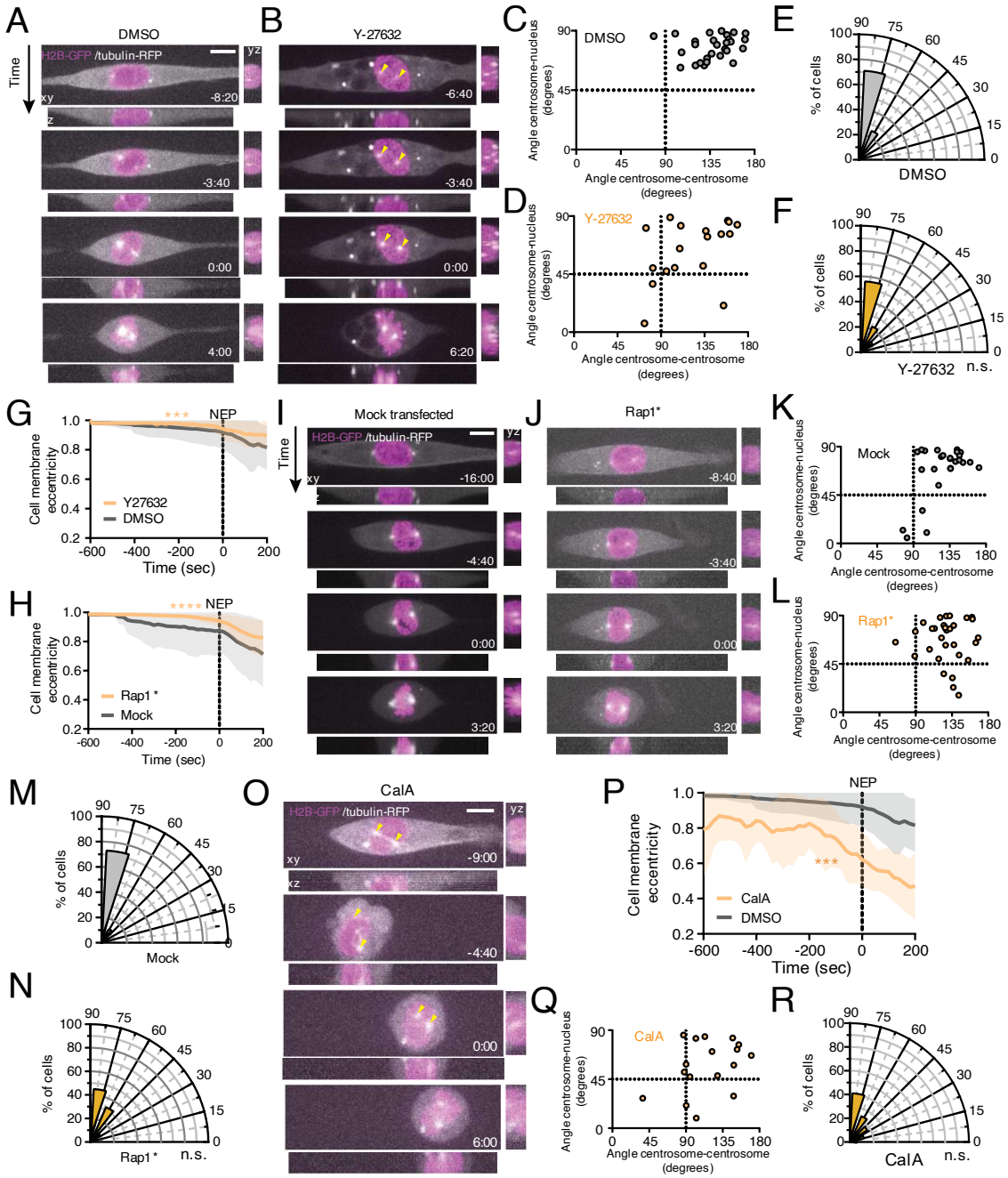

Figure 2 - Cell rounding status does not influence centrosome positioning in RPE-1 cells.

Representative frames from a movie of an RPE-1 cell stably expressing H2B-GFP and RFP-tubulin, seeded on a 10µm wide-micropatterned line, treated with **(A)** DMSO and **(B)** Y-27632, showing centrosome movement. Time min:sec. Time zero corresponds to NEP. Scale bar = 10µm. Yellow arrows indicate centrosome position. Correlation between centrosome separation (angle centrosome-centrosome; x axis; n.s. – not significant) and centrosome positioning (angle

centrosome-nucleus; y axis;), at the moment of NEP, for DMSO-treated control RPE-1 cells (C; n=28) and Y-27632-treated ones (D; n=18). Polar plot quantifying centrosome positioning relative to the longest nuclear axis at NEP for these RPE-1 cells treated with **(E)** DMSO or **(F)** Y-27632. **(G)** Quantification of cell membrane eccentricity of DMSO-treated cells (gray) and Y-27632-treated cells (orange; ****p<0.001). Dashed line represents moment of NEP. See also Fig. S2. **(H)** Quantification of cell membrane eccentricity of mock transfected (Mock; gray; n=25) and Rap1* transfected cells (orange; n=31; ****p<0.001). Dashed line represents moment of NEP. Representative frames from movies of mock **(I)** and Rap1* **(J)** transfected RPE-1 cells, stably expressing H2B-GFP and RFP-tubulin, seeded on a 10µm wide-micropatterned line. Time is in min:sec. and time zero corresponds to NEP. Scale bar = 10µm. See also Fig. S2. Correlation between centrosome separation to opposite sides of the nucleus (angle centrosome-centrosome; x axis) and centrosome positioning relative to the shortest nuclear axis (angle centrosome-nucleus; y axis), at the moment of NEP for Mock (**K**; n=26) and Rap1* (**L**; n=31) transfected cells. Polar plot quantifying centrosome positioning relative to the longest nuclear axis at NEP for Mock **(M)** or Rap1* **(N;** n.s. – not significant) transfected RPE-1 cells. **(O)** Frames from a representative movie of a CalyculinA (CalA) treated RPE-1 cell, stably expressing H2B-GFP and RFP-tubulin, seeded on a 10µm wide-micropatterned line. Time min:sec. Time zero corresponds to NEP. Scale bar = 10µm. **(P)** Quantification of cell membrane eccentricity of CalA-treated cells (orange; n=17; ****p<0.001). Dashed line represents moment of NEP. **(Q)** Correlation between centrosome separation to opposite sides of the nucleus (angle centrosome-centrosome; x axis; n.s. – not significant) and centrosome positioning on the shortest nuclear axis (angle centrosome-nucleus; y axis) at the moment of NEP, for cells treated with CalA. **(R)** Polar plot quantifying centrosome positioning relative to the longest nuclear axis at NEP for cells treated with CalA (n.s. – not significant).

To further investigate the impact of cell rounding for centrosome positioning, we then decided to interfere with mitotic cell rounding in the U2-OS and MDA-MB-468 cancer cell lines. We either forced adhesion in the highly rounded MDA-MB-468 or promoted rounding in the flatter U2-OS cells. We started by transfecting MDA-MB-468 cells with Rap1*. As expected, Rap1* expression delayed cell rounding (Fig. S2A, B), but this did not restore correct centrosome separation or positioning (Fig. S2C, D). Next, we tried to interfere with rounding in U2-OS cells by using Y-27632 or CalA (Fig. S2E-I). Neither treatment was sufficient to restore centrosome positioning on the shortest nuclear axis

(Fig. S2J-M)**.** Because these results were obtained from cells seeded on micropatterned lines with 10μm width, we also wanted to rule out the possibility that the failure to position centrosomes could be due to geometrical constraints imposed by the micropattern. Therefore, we seeded U2-OS cells on micropatterned lines with 20μm width or on non-patterned FBN-coated coverslips. In all these conditions, U2-OS cells were still unable to correctly position their centrosomes at the shortest nuclear axis (Fig. S2N-S), even though they showed a significantly decrease in cell membrane eccentricity when placed in non-patterned substrates, reflecting a more rounded state (Fig. S2T; ****$p<0.0001$). Taken together, our results indicate that centrosome positioning on the shortest nuclear axis in normal, untransformed RPE-1 cells is independent of the rounding state of the cell and that the defects in positioning observed in the U2-OS and MDA-MB-468 cancer cells cannot be rescued by manipulating cell rounding.

The nuclear lamina is not required for centrosome positioning on the shortest nuclear axis

Given these results and our previous observations[23], it seems unlikely that an external cue could be driving centrosome positioning during early mitosis. Therefore, we hypothesized that a nuclear cue could be responsible for ensuring accurate centrosome positioning on the shortest nuclear axis. One possible candidate is the nuclear lamina, since it was previously shown that lamins can position NPCs and centrosomes[27] and are required for centrosome separation[28]. We started by analysing the levels of nuclear lamina components in each of the cell lines in our panel, by measuring the fluorescence intensity of lamin A/C and lamin B1 at the NE (Fig. S3A, B). We observed that the levels

of both Lamin A/C and Lamin B1 were altered in U2-OS and MDA-MB-468, when compared to RPE-1 cells (Fig. S3C, D). Consequently, the ratios of lamin A/C relative to lamin B1 in the two cancer cell lines were substantially lower than in RPE-1 cells (Fig. S3E; ****$p<0.001$). Our results are in agreement with lamin expression data available from the online repository Cancer Dependency Map Project (DepMap) (Fig. S3F). Moreover, the decrease in lamin A levels observed in cancer cells was accompanied by a decrease in nuclear solidity (Fig. S3G, **** $p<0.001$), which suggests that nuclear structure in both U2-OS and MDA-MB-468 cells is altered when compared to RPE-1 cells. Thus, we decided to manipulate lamin levels in RPE-1 cells and ask whether this was sufficient to impair centrosome positioning on the shortest nuclear axis. We started by depleting Lamin A in RPE-1 cells, using RNA interference (siLMNA; Fig. 3A-C). However, this depletion was not sufficient to alter centrosome behaviour, as cells still efficiently separated and positioned them at the shortest nuclear axis (Fig. 3D-G). To confirm our observations, we next sought to imbalance the lamin A:B ratio by overexpressing a HaloTag9-Lamin B1 construct in RPE-1 cells (Fig. 3H, I). Similarly to Lamin A depletion, Lamin B1 overexpression also did not disrupt correct centrosome positioning at NEP (Figure 3J-M). Taken together, these results indicate that even though the ratio of lamin A:B is perturbed in the two cancer cells used for this study, this is likely not the cause for the observed errors in centrosome positioning at NEP, as experimental manipulation of the levels of either lamin A or B in RPE-1 cells did not affect this process.

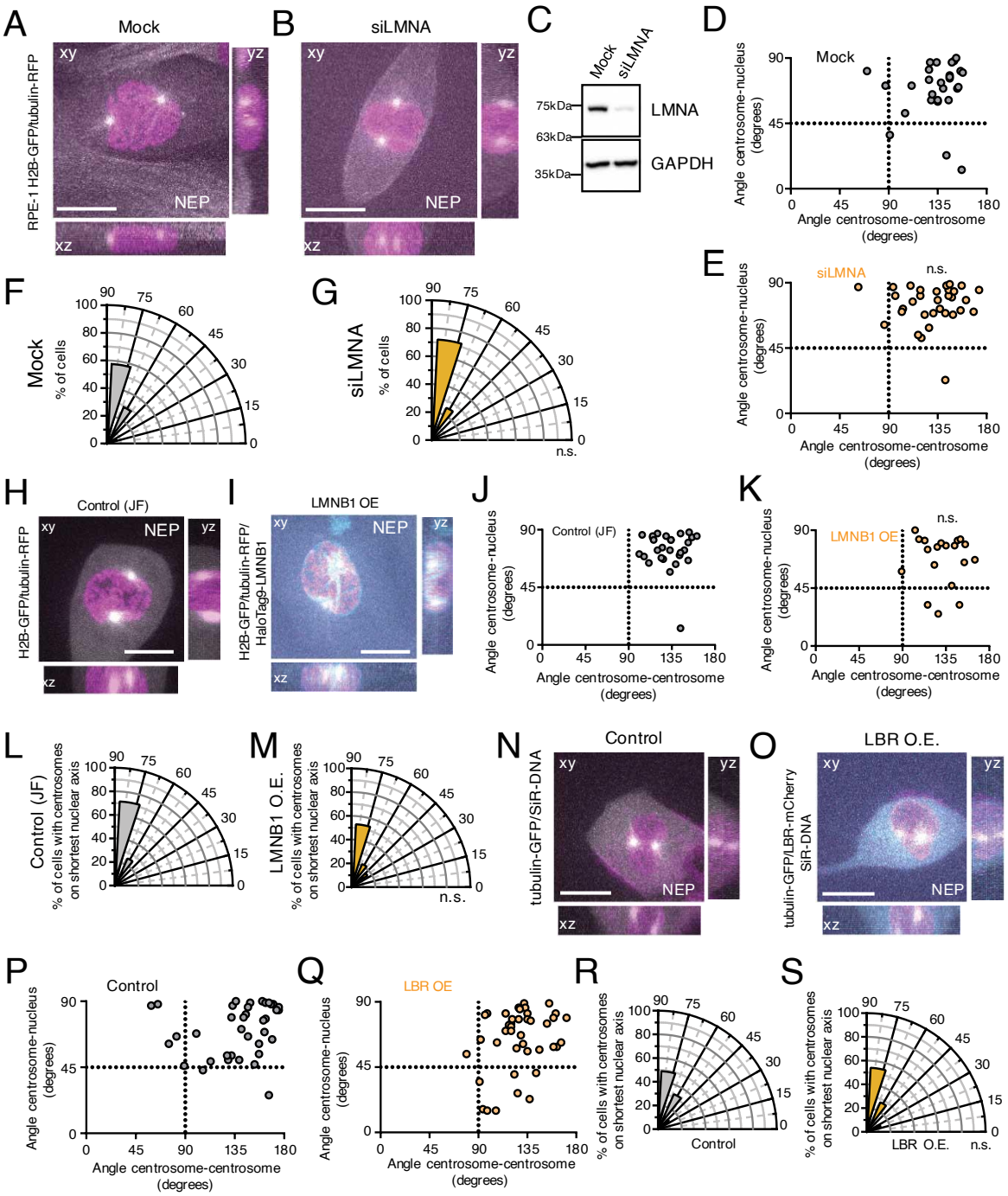

Figure 3 – Nuclear lamina components do not affect centrosome positioning

Representative frames from movies of Mock **(A)** or Lamin A depleted **(B;** siLMNA) RPE-1 cells at the moment of NEP, stably expressing H2B-GFP and RFP-tubulin. Scale bar=10µm. **(C)** Western blot showing depletion efficiency for these cells. Correlation between centrosome separation (angle centrosome-centrosome; x axis; n.s. – not significant) and centrosome positioning (angle centrosome-nucleus; y axis) at the moment of NEP, for Mock (**D**; n=28) and Lamin A

depleted (**E**; n= 32) cells. Polar plots quantifying centrosome positioning relative to the longest nuclear axis at NEP for Mock **(F)** and LMNA depleted RPE-1 cells (**G**; n.s. – not significant). See Fig. S3. Representative frame of the moment of NEP from movies of RPE-1 cells stably expressing H2B-GFP and RFP-tubulin (**H**; control treated with JF647; n=28) or overexpressing HaloTag9-LMNB1 (**I**; LMNB1 OE; n=19). Scale bar = 10µm. Correlation between centrosome separation (angle centrosome-centrosome; x axis) and centrosome positioning (angle centrosome-nucleus; y axis; n.s. – not significant) at the moment of NEP, for Control cells **(J)** and cells overexpressing LMNB1 **(K)**. See Fig. S3. Polar plots quantifying centrosome positioning relative to the longest nuclear axis at NEP for Control **(L)** and LMNB1 overexpressing RPE-1 cells (**M;** n.s. – not significant). Representative frames of the moment of NEP from movies of Control (**N**; n=37) or LBR-mCherry overexpressing (**O**; n=41) RPE-1 cells, stably expressing GFP-tubulin and treated with SiR-DNA, plated on fibronectin. Scale bar = 10µm. See Fig. S3. Correlation between centrosome separation (angle centrosome-centrosome; x axis) and centrosome positioning (angle centrosome-nucleus; y axis; n.s. – not significant) at the moment of NEP, for Control **(P)** and LBR overexpressing **(Q)** cells. Polar plots quantifying centrosome positioning relative to the longest nuclear axis at NEP for Control **(R)** and LBR overexpressing RPE-1 cells (**S**; n.s. – not significant).

Next, we sought to interfere with additional nuclear components, independently of lamin levels. To do so, we overexpressed an mCherry-tagged version of lamin B receptor (LBR), an integral protein of the inner nuclear membrane (INM) that associates with the nuclear lamina[43]. It has been previously shown that LBR overexpression causes perinuclear ER expansion and the overproduction of nuclear membranes[44], leading to NE folding and altered nuclear structure[45], similar to what we observed in U2-OS and MDA-MB-468 cells. However, interfering with nuclear structure by overexpressing LBR in RPE-1 cells (Fig. 3 N, 3O), did not affect the separation and positioning of centrosomes on the shortest nuclear axis (Fig. 3P-S).

Overall, our data indicates that neither the nuclear lamina nor LBR are required for correct centrosome positioning during early mitosis. They further suggest that the altered lamin

levels in U2-OS and MDA-MB-468 are likely not the cause for the mispositioned centrosomes observed in these cell lines.

The LINC complex is required for centrosome positioning on the shortest nuclear axis

Next, we focused our attention on the LINC complex, since it was previously shown to play a role in early mitosis[33,34]. Immunolocalization of SUN1 and SUN2 in prophase cells revealed that both proteins localized to the NE, as expected (Fig. 4A, B). Interestingly, in a significant proportion of cells, SUN1 and SUN2 also concentrated in the area between and around the two separating centrosomes and their corresponding microtubule arrays (Fig. 4A, B, insets). This localization was dependent on microtubules, since treatment with low doses of nocodazole (Noc) disrupted inter-centrosomal SUN localization (Fig. 4C, D). We then proceeded by depleting individual SUN proteins (SUN1 and SUN2), in RPE-1 cells using a lentiviral-mediated short hairpin RNA (shRNA), giving rise to a heterogeneous population of cells with different levels of depletion (Fig. 4A, B and Fig. S4A-D). This was sufficient to decrease NE localization and inter-centrosomal accumulation of SUN1 and SUN2 (Fig. 4A, B). We then assessed the impact of SUN1 and SUN2 depletion for centrosome behaviour throughout mitotic entry. Upon depletion, these cells were still capable of efficiently separating centrosomes (Figure 4E-J, angle centrosome-centrosome; Sup. movies S4 and S5). However, they did not place the centrosomes at the shortest nuclear axis (Figure 4K-M; *p=0.0165 and p=0.0175 for SUN1 and SUN2, respectively).

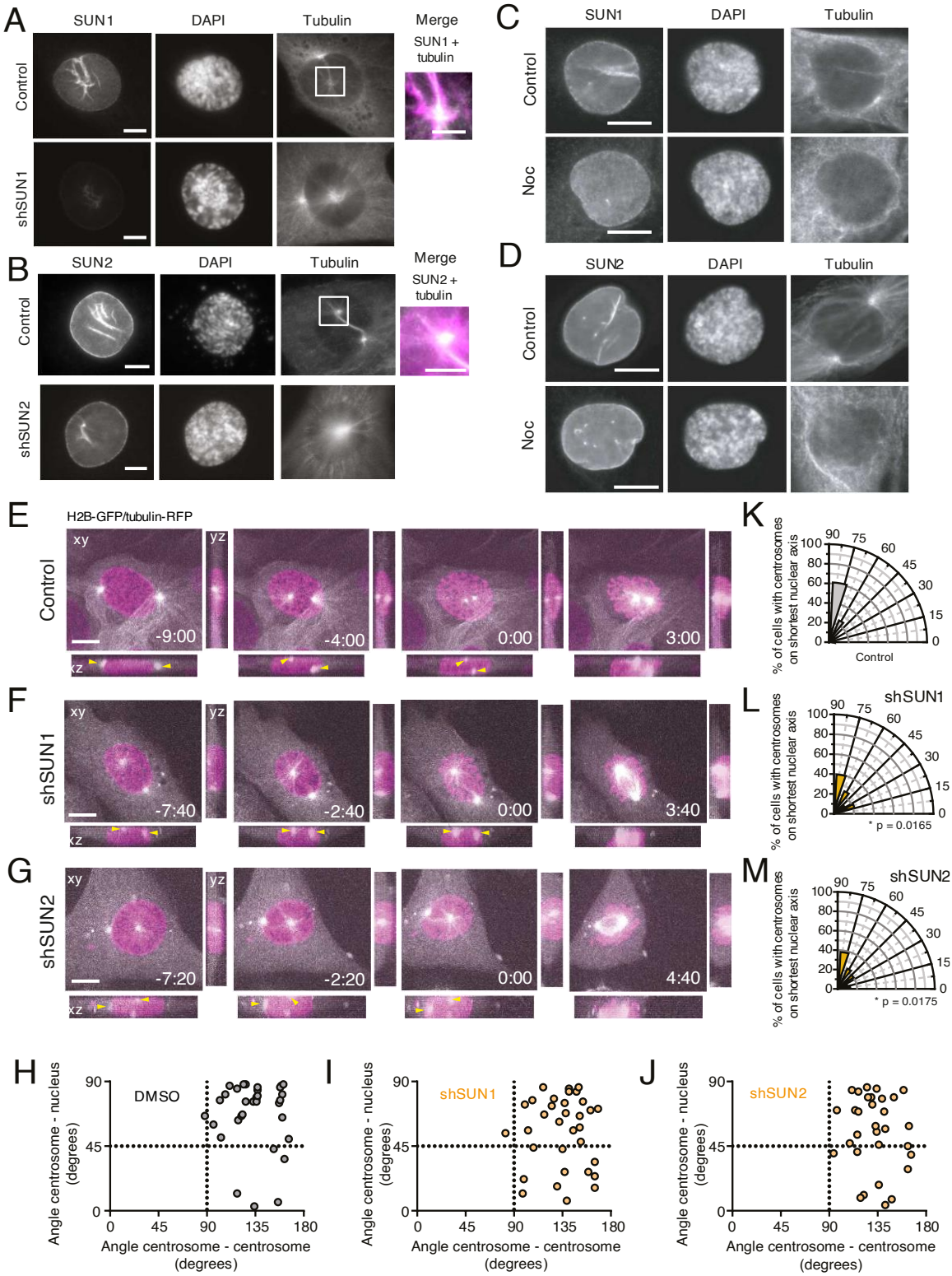
A
SUN1
DAPI
Tubulin
Merge
SUN1 + tubulin
Control
shSUN1
B
SUN2
DAPI
Tubulin
Merge
SUN2 + tubulin
Control
shSUN2
C
SUN1
DAPI
Tubulin
Control
Noc
D
SUN2
DAPI
Tubulin
Control
Noc
E
H2B-GFP/tubulin-RFP
Control
xy
yz
xz
-9:00
-4:00
0:00
3:00
F
shSUN1
-7:40
-2:40
0:00
3:40
G
shSUN2
-7:20
-2:20
0:00
4:40
K
% of cells with centrosomes on shortest nuclear axis
Control
L
shSUN1
* p = 0.0165
M
shSUN2
* p = 0.0175
H
DMSO
I
shSUN1
J
shSUN2
Angle centrosome - nucleus (degrees)
Angle centrosome - centrosome (degrees)

Figure 4 – SUN proteins are required for correct centrosome positioning.

(A) Representative immunofluorescence images of Control and shSUN1 treated cells, immunostained for SUN1. **(B)** Representative immunofluorescence images of Control and shSUN2 treated cells cells, immunostained for SUN2. Scale bar = 10µm. Note the co-localisation between tubulin and the SUN proteins in the merged image inset. See Fig. S4. Representative immunofluorescence images of Control and shSUN1-treated RPE-1 cells **(C)** or Control and shSUN2-treated cells **(D)**. Nocodozole (Noc) was added to the cells for 10 minutes, to induce microtubule depolymerisation. Note the decrease in SUN1 and SUN2 staining between the centrosomes. Representative frames from movies of Control **(E)**, shSUN1-treated **(F)** or shSUN2-treated **(G)** cells, stably expressing H2B-GFP and RFP-tubulin, seeded on fibronectin, during mitotic entry. Time min:sec. Time zero corresponds to NEP. Scale bar = 10µm. Yellow arrows indicate centrosomes position. . Correlation between centrosome separation (angle centrosome-centrosome; x axis) and centrosome positioning (angle centrosome-nucleus; y axis) at the moment of NEP, for Control cells (**H**; n= 33), shSUN1-treated (**I**; n= 33), and shSUN2-treated (**J**; n= 31) cells. Polar plots quantifying centrosome positioning relative to the longest nuclear axis at NEP for Control **(K)**, shSUN1-treated (**L**; *p=0.0165), and shSUN2-treated (**M**; * p=0.0175) cells.

Given the results obtained with SUN1 and SUN2, we then tested whether nesprins, which are part of the LINC complex and interact with SUN proteins in the perinuclear space, could also impact centrosome function. For that purpose, we expressed a dominant-negative form of KASH tagged with mCherry (DN-KASH; Fig. 5A, B; Sup. Movie S6 and S7) that prevents its binding to SUN proteins and blocks force propagation across the NE[46,47]. As a corresponding control, we generated a cell line expressing a mCherry-tagged mutant version of the same DN-KASH construct where the last 4 aminoacids (PPPL) of the KASH domain were removed (ΔPPPL-KASH). This prevents ΔPPPL-KASH from interacting with SUN1 or SUN2, thus making it a “defective” dominant negative[47]. Firstly, we confirmed by immunofluorescence the ability of the DN-KASH construct

displace endogenous nesprins from the NE, as assessed by nesprin 2 localization (Fig. 5C; SYNE-2).

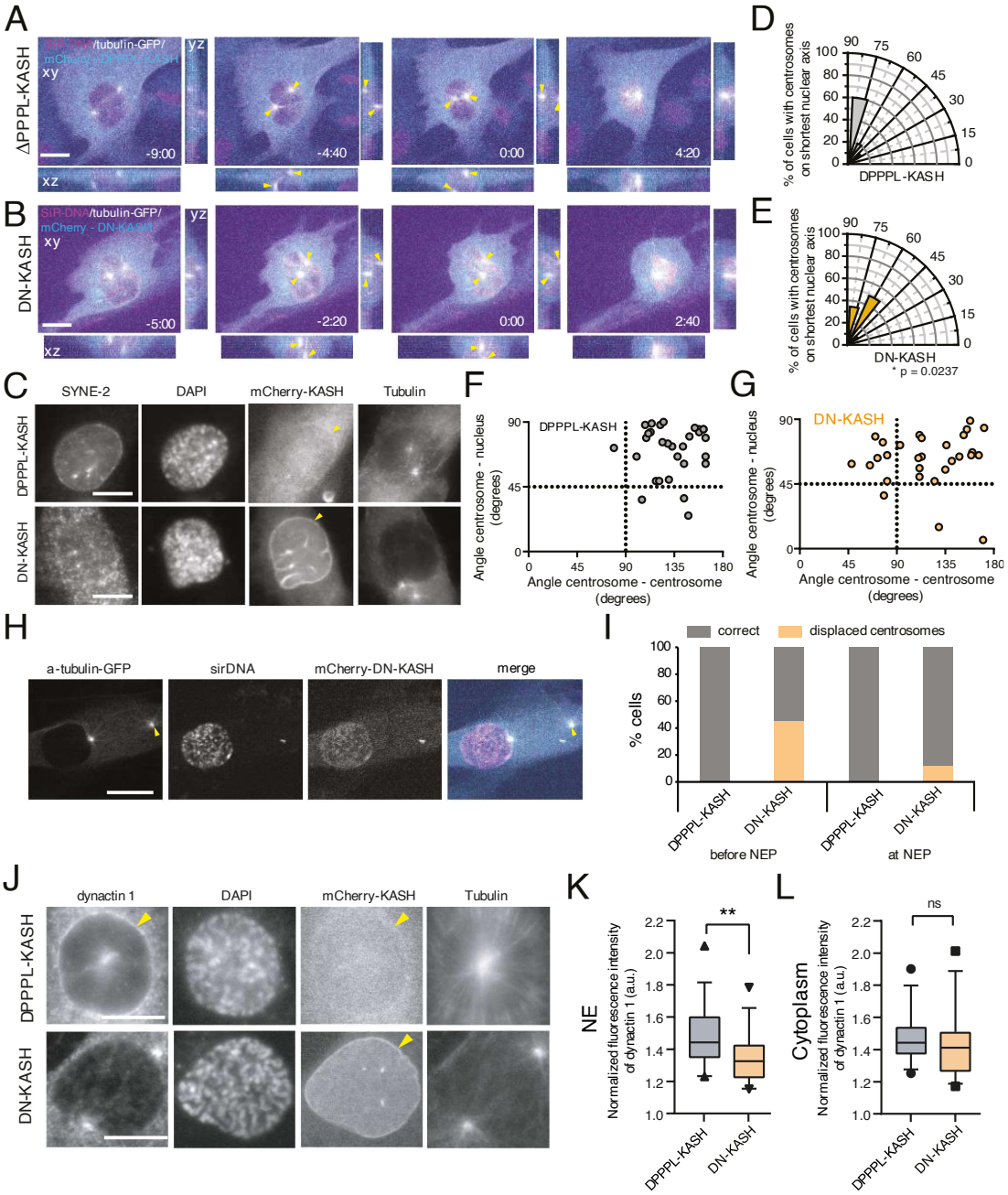

Figure 5 – The LINC complex is required for centrosome positioning on the shortest nuclear axis.

Representative frames from movies of Control (**A**; ΔPPPL-KASH) and DN-KASH **(B)** treated cells, stably expressing tubulin-GFP and treated with SiR-DNA, seeded on fibronectin, during mitotic entry. Time min:sec. Time zero

corresponds to NEP. Scale bar=10µm. Yellow arrows indicate centrosomes position. See. Fig. S4. **(C)** Representative immunofluorescence images of a ΔPPPL-KASH (top panel) and a DN-KASH (bottom panel) cell, immunostained for nesprin-2 (SYNE-2). Note how expression do DN-KASH displaces nesprin-2 from the NE (yellow arrows), as opposed to expression of ΔPPPL-KASH. Polar plots quantifying centrosome positioning relative to the longest nuclear axis at NEP for RPE-1 expressing ΔPPPL-KASH (**D**; n= 30) or DN-KASH cells (**E**; n= 29; *p=0.0237). Correlation between centrosome separation (angle centrosome-centrosome; x axis) and centrosome positioning (angle centrosome-nucleus; y axis) at the moment of NEP for Control (**F**; ΔPPPL-KASH) or DN-KASH expressing **(G)** cells. **(H)** Representative frame from a movie of a DN-KASH expressing cell, stably expressing Tubulin-GFP and treated with SiR-DNA, highlighting centrosome detachment from the NE (yellow arrow). **(I)** Quantification of centrosome displacement from the NE during mitotic entry for ΔPPPL-KASH or DN-KASH expressing cells before and at NEP. **(J)** Representative immunofluorescence images of ΔPPPL-KASH or DN-KASH cells, labelled for the dynein adaptor, dynactin1. Please note the decreased dynactin1 signal at the NE of DN-KASH expressing cells, when comparing to the ΔPPPL-KASH controls. Quantification of the normalized fluorescence intensity signal of dynactin 1 signal on the NE **(F;** **p<0.01**)** and cytoplasm **(G)** of ΔPPPL-KASH (n= 36) or DN-KASH (n= 35) cells.

Contrarily, and as expected, expression of the ΔPPPL-KASH construct did not interfere with nesprins localization on the NE (Fig. 5C). We then analysed centrosome behaviour in these cells. Upon expression of ΔPPPL-KASH, cells behaved similarly to unmanipulated RPE-1 cells, with an efficient separation and positioning of centrosomes on the shortest nuclear axis (Fig. 1C, 5D-G; n.s. – not significant). However, DN-KASH-expressing cells showed compromised separation and positioning of centrosome (Fig. 5D-G, * p=0.0155 and * p=0.0237, respectively). Overall, our data strongly indicates that the LINC complex provides the cues for positioning centrosomes on the shortest nuclear axis during prophase.

Dynein recruitment to the NE during early mitosis requires a functional LINC complex

Next, we sought to determine how LINC complex disruption affected centrosome positioning during prophase. While imaging DN-KASH-expressing cells, we frequently observed centrosome detachment from the NE during earlier stages of prophase (Fig. 5H, 5I), which was never observed in cells expressing the ΔPPPL-KASH construct (Fig. 5I) or unmanipulated RPE-1 cells. Curiously, this centrosome displacement from the NE decreased as cells entered mitosis (Fig. 5I). These observations suggest that disruption of the LINC complex leads to a transient defect in centrosome-NE tethering during the G2-M transition, which is rescued as cells approach NEP. Previous studies have shown that a specific pool of NE-bound dynein, is sufficient to tether centrosomes to the NE during prophase, by generating pulling forces on microtubules[48,49], in a BicD2[32] or Nup133-dependent manner[50]. Moreover, the LINC complex was previously shown to help maintain the centrosome-nucleus connection during neuronal migration in mice[30]. Thus, we decided to analyse whether the centrosome displacement we observed in DN-KASH cells could be due to a defective loading of dynein on the NE, triggered by a disruption of the LINC complex. For this purpose, we assessed the localization of dynactin 1, a dynein adaptor that also localizes to the NE[51], upon expression of ΔPPPL-KASH or DN-KASH. Importantly, expression of DN-KASH significantly decreased the levels of dynactin 1 on the NE, when compared to cells expressing ΔPPPL-KASH (Fig. 5J, K; ** $p<0.01$), while having no effect on the overall levels of cytoplasmic dynactin 1 (Fig. 5L). Our results indicate that an intact LINC complex is required for dynein localization at the NE during the G2-M transition, which then allows accurate centrosome positioning at NEP.

A compromised LINC complex impacts mitotic fidelity

Finally, we sought to understand the functional implication of disrupting LINC complex-mediated centrosome positioning for chromosome segregation accuracy. As mentioned before, incomplete centrosome separation leads to erroneous kinetochore-microtubule attachments, resulting in increased chromosome segregation defects[20,22,23]. Considering our observations implicating the LINC complex on the loading of NE-dynein and centrosome-nucleus axis orientation at NEP, we now determined whether LINC complex disruption could be sufficient to trigger chromosome segregation errors. To do so, we imaged RPE-1 cells expressing H2B-GFP and tubulin-RFP throughout an entire mitosis, in the presence or absence of LINC complex components and analysed mitotic progression and chromosome segregation (Fig. 6A). In control RPE-1 cells, mitosis progresses with residual levels of chromosome missegregation events, within 20±2.8min min (Fig. 6A-D and Fig. S6A). Upon depletion of SUN1, cells showed a significant increase in chromosome segregation errors (approximately 40% of all filmed cells), which consisted mainly of lagging DNA (Fig. 6A, B; ****$p<0.001$). Moreover, these cells showed a slight delay between NEP and metaphase (Fig. 6C, D and Fig. S6A; **$p=0.009$). Curiously, this increased rate of chromosome missegregation is comparable to the ones observed in U2-OS and MDA-MB-468 cell lines (Fig. S6B; ***$p<0.01$). Depletion of SUN2, on the other hand, did not increase chromosome segregation defects (Fig. 6B), or delayed mitotic progression (Figure 6C, D and Fig. S6A). These results are different from a previous report showing that SUN2 depletion induced a mitotic delay[52]. However, it should be noted the Belaadi and colleagues used HeLa cells, which have significantly different expression levels of both SUN1 and SUN2 compared to the RPE-1 cells used in our

study[53]. These may reflect different cellular dependencies on individual SUN proteins which warrant further investigation.

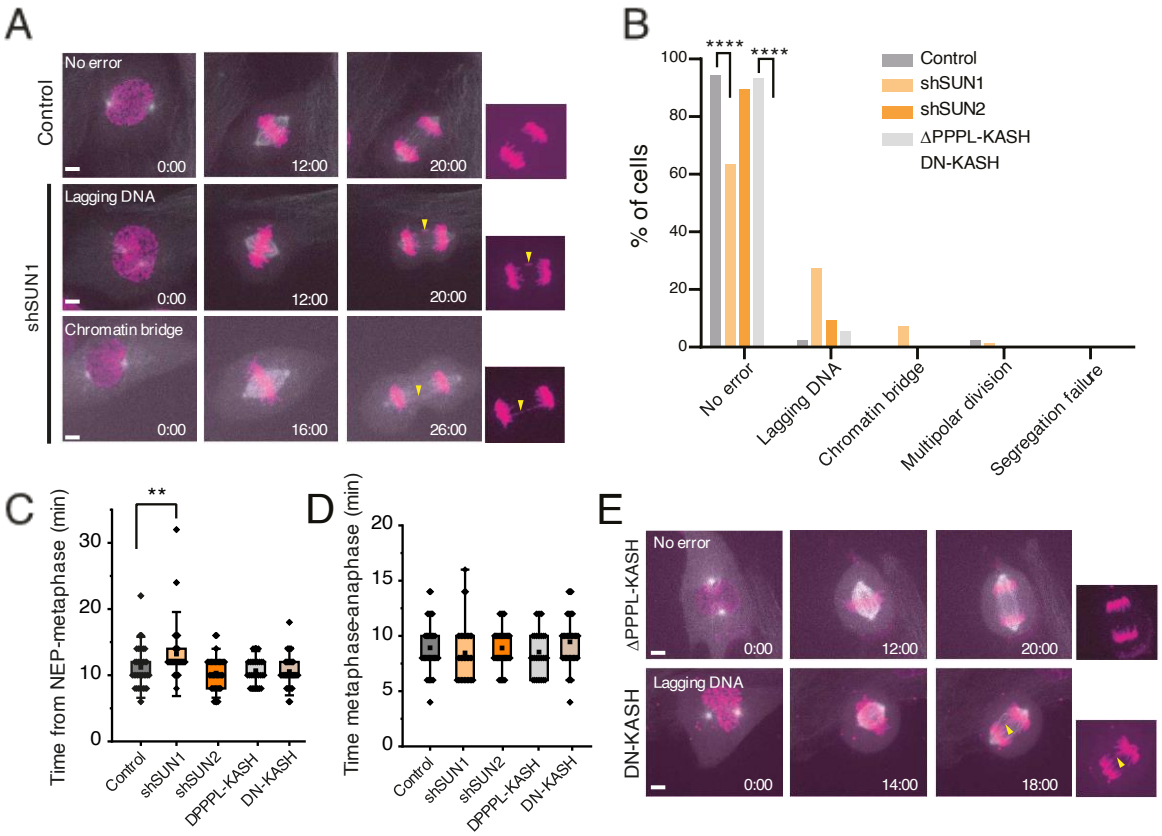

Figure 6 – LINC complex disruption increases rates of chromosome segregation.

(A) Representative frames from movies of Control and shSUN1-treated cells, stably expressing H2B-GFP and RFP-tubulin and seeded on fibronectin. Please note the different chromosome missegregation phenotypes (yellow arrows, insets). Time min:sec. and time zero corresponds to NEP. Scale bar=10µm. **(B)** Quantification of anaphase segregation events of RPE-1 Control (n= 39), shSUN1 (n= 39; ****p<0.001), shSUN2 cells (n= 40), ΔPPPL-KASH (n= 32) and DN-KASH (n= 38; ****p<0.001) cells, seeded on fibronectin. Quantification of the time from NEP to metaphase **(C)**, and metaphase to anaphase **(D)**, in minutes. See Fig. S5. **(E)** Representative frames from movies of Control (ΔPPPL-KASH) and DN-KASH cells, stably expressing tubulin-GFP and treated with SiR-DNA, seeded on fibronectin. Please note the chromosome missegregation phenotype (yellow arrow, inset). See Fig. S5.

Finally, we decided to test whether expression of DN-KASH, which affects centrosome positioning (Fig. 5A-D), would also impact mitotic progression and chromosome segregation. Expression of DN-KASH significantly increased chromosome segregation defects, when compared to ΔPPPL-KASH (Fig. 6B, E; ****$p<0.001$), without changing mitotic timings (Fig. 6C, D). Taken together, our results indicate that an intact LINC complex is important to ensure accurate chromosome segregation.

DISCUSSION

The manner in which centrosomes separate and position during prophase has direct implications for the efficiency of mitosis[20,22,33]. We previously reported that, during the G2-M transition, separating centrosomes exhibit a coordinated motion along the NE, so that they are positioned on the shortest nuclear axis at the moment of NEP[23]. This centrosome-nucleus configuration occurs independently of the cortical cues that dictate spindle orientation in later stages of mitosis, since these cortical complexes are only assembled after NEP[54,55]. Importantly, this prophase configuration suggested that a nuclear signal could be providing the cues to regulate centrosome positioning during the early stages of mitosis. However, the molecular mechanism remained unclear. Here, we show that this centrosome-nuclear axis orientation is a robust, LINC complex-dependent process in near-diploid, untransformed RPE-1 cells and that this mechanism is disrupted in the U2-OS and MDA-MB-468 cancer cell lines (Fig. 1).

In preparation for mitosis, most cells round up and adopt a spherical shape[56]. This event, driven by a combination of adhesion disassembly[3] and membrane retraction[8], is required

to release the geometric constraints imposed by cell shape[37,39]. In addition, this allows nuclear rotation during prophase[23] and provides sufficient space for mitotic spindle assembly to occur without errors[39,57]. Interestingly, we observed significant changes in the coordination between cell rounding and NEP in the cancer cell lines (Fig. 1A-I), which resulted in an impairment of nuclear rotation and centrosome positioning. We hypothesized that abnormal cell rounding could be responsible for the defects in centrosome positioning that we observed in the cancer cell lines. However, interfering with cell rounding in RPE-1 cells, either by delaying it or accelerating it, did not disrupt accurate centrosome positioning. These observations rule out mitotic cell rounding as the main driver of centrosome positioning in early mitosis and reinforce the efficiency of centrosome-nuclear axis orientation in RPE-1 cells. In addition, they also suggest that the cues instructing centrosome positioning emanate from the nucleus. Using the nucleus as a positional cue during early mitosis has significant advantages. This would allow centrosomes to orient correctly under conditions where external cues are mostly absent, due to the disassembly of adhesion complexes in late G2[3,58] and before the cortical loading of the LGN-Gα1-NuMa complex, which occurs only in prometaphase[54,55]. In addition, this configuration would also enable the efficient assembly of a spindle scaffold[23], ensuring a faster capture of kinetochores and mitotic progression[20,22,23].

Many nuclear components could serve as potential candidates to influence centrosome behaviour. The LINC complex, due to its localization bridging the nucleus and cytoplasm, is ideally placed to perform this function. Accordingly, it is involved in centrosome-nucleus tethering and nuclear migration in C. elegans[59] and myotubes[60,61], and was also shown to affect multiple aspects of mitotic progression[33,34,52,62]. However, the molecular

mechanism behind LINC complex-mediated centrosome positioning during the early stages of mitosis remained unclear. One likely possibility is that, during late G2, the LINC complex could be directly involved in the recruitment of dynein to the NE. It is well established that during this stage, two parallel and independent nucleoporin-mediated pathways regulate dynein NE loading[63]. Upon phosphorylation by CDK1[64], the nucleoporin RanBP2 binds to BicD2, leading to dynein recruitment[32,65]. Additionally, Nup133 recruits CENP-F, which then binds NudE/NudEL to load dynein on the NE[50]. Once at the NE, dynein generates pulling forces on microtubules which results in centrosomes tethering to the nucleus, aiding centrosome separation[19] and facilitating NEP[66,67]. Here, we show that in untransformed RPE-1 cells, the LINC complex acts during late G2 to assist in NE-dynein loading (Fig. 5) and provide spatial cues for centrosome positioning (Fig. 4 and 5), in parallel with the NPC-mediated pathways. These observations fit nicely with a previous report showing a role for the LINC complex in centrosome movement during early mitosis[33]. In addition, LINC complex components SUN1 and SUN2, which are located on the inner nuclear membrane, were also shown to interfere with spindle assembly by delaying the removal of membranes from chromatin [52,68]. Together with our results, these observations indicate that the LINC complex acts on multiple levels during early spindle assembly. By assisting in the recruitment of NE-dynein, it ensures the accurate positioning of centrosomes on the shortest nuclear axis, to allow faster assembly of the mitotic spindle. In line with this hypothesis, we and others have shown that disruption of the LINC complex, while unable to block mitotic entry, induces a severe delay in the process by decreasing the rate of cyclin B1 nuclear accumulation[45] and interfering with spindle assembly efficiency[33,34,68]. In parallel, by

facilitating the removal of membranes from chromatin[68], it also accelerates the capture of kinetochores by microtubules. Overall, this would result in a more efficient “search and capture” of chromosomes during early prometaphase which, together with the "ring-like” distribution of chromosomes[62], ensures a maximum exposure of kinetochores to microtubules and decreases the probability of generating of erroneous kinetochore-microtubule attachments[69,70]. Notably, mutations and abnormal expression of LINC complex proteins have been implicated in a plethora of cancers[71–73], suggesting a potential role in the maintenance of chromosomal stability. However, additional work is required to determine the exact molecular nature of the spatial cues that drive centrosome movement to the shortest nuclear axis. One hypothesis is that asymmetric localization of force-generating complexes on the NE could bias centrosome movement to a specific nuclear orientation. Accordingly, we observed an accumulation of SUN proteins in nuclear areas between the separating centrosomes, in a microtubule-dependent manner (Fig. 4).

Overall, we propose a model in which LINC complex-mediated loading of dynein at the NE dictates centrosome positioning at the shortest nuclear axis upon NEP and this is required to ensure accurate spindle assembly and efficient chromosome segregation in human cells.

Acknowledgments:

This work was funded by Portuguese funds through FCT—Fundação para a Ciência e a Tecnologia/Ministério da Ciência, Tecnologia e Ensino Superior in the framework of the project PTDC/BIA-CEL/6740/2020. J.T.L. is supported by grant SFRH/BD/147169/2019

from FCT. The authors thank Helder Maiato for critical reading of the manuscript and access to essential equipment for live cell imaging. Work in the Maiato lab is funded by the European Research Council consolidator grant CODECHECK, under the European Union's Horizon 2020 research and innovation programme (grant agreement 681443), Fundação para a Ciência e a Tecnologia of Portugal (PTDC/MED-ONC/3479/2020) and La Caixa Health Research Grant (LCF/PR/HR21/52410025). The authors would like to thank Tom Misteli for the Halo-Tag9-LaminB1 plasmid, Jean de Gunzburg for the pRK5-Rap1[Q63E] construct and Stephen Royle for the plasmid pWPT LBR-mCherry.

Author contributions:

J.T.L. performed experimental work, analysed data, prepared figures and wrote the manuscript. J.G.F. provided the conceptual framework, prepared figures, wrote the manuscript and provided funding.

Declaration of interests:

The authors declare no competing interests.

Materials and Methods

Cell lines

RPE-1, U2-OS and MDA-MB-468 cell lines were cultured in DMEM (Life Technologies) supplemented with 10% FBS (Fetal Bovine Serum; Life Technologies) and kept in culture in a 37ºC humidified incubator with 5% CO_2. For MDA-MB-468 cells, media was also supplemented with GlutaMAXÊ (Life Technologies). RPE parental, RPE H2B-GFP/mRFP-α-tubulin, U2OS parental, U2OS H2B-GFP/mRFP- α-tubulin and MDA-MB-468 parental were already available in our lab. RPE-1 α-tubulin-GFP, RPE-1 α-tubulin-GFP/LBR-mCherry and MDA-MB-468 H2B-GFP/mRFP-α-tubulin cell lines were generated by transduction with lentiviral vectors containing the respective plasmids available in our lab – Table 1. For this purpose, we used HEK293T cells at a 50-70% confluence that were co-transfected with lentiviral packaging vectors (16.6μg of Pax2, 5.6μg of pMD2 and 22.3μg of the plasmid of interest), using 30μg of Lipofectamin 2000 (Life Technologies). Approximately 48 hours after transfection, the virus-containing supernatant was collected, filtered, and stored at -80ºC. Cells were infected with the collected virus together with polybrene (1:1000) in standard culture media for 24h. Some days after the infection, the cells expressing the fluorescent tags were isolated by fluorescence activated cell sorting (FACS; FACS Aria II).

RPE-1 H2B-GFP/mRFP-α-tubulin/shSUN1 and RPE-1 H2B-GFP/mRFP-α-tubulin/shSUN2 were also generated by infecting cells, using commercially available lentiviral vectors encoding the desired shRNAs (MISSION® shRNA, Sigma-Aldrich; shSUN1 - TRCN0000133901 - Target Sequence: CAGATACACTGCATCATCTTT;

shSUN2 - TRCN0000141958 - Target Sequence: GCAAGACTCAGAAGACCTCT). Cells were then selected with puromycin (20μg/mL; Merck Millipore) for 7 days. RPE-1 cells expressing the KASH constructs were generated via lentiviral infection. RPE-1 α-tubulin-GFP cells were infected with viruses containing the mCherry-DN-KASH or mCherry-DN-KASHΔPPPL plasmids, as described previously. Doxycycline (5μg/ml; Fischer Scientific) was added for 24h to the culture media to stimulate the expression of the different KASH fusion proteins. After this period, the cells expressing the fluorescent tags were isolated by FACS and placed back in normal media for expansion. Addition of doxycycline was performed again 24 hours before imaging. RPE-1 H2B-GFP/mRFP-α-tubulin/Halo-Tag9-LaminB1 cell line was generated by transiently transfecting a HaloTag9-LaminB1 plasmid (gift from Tom Misteli) using Lipofectamin 2000 (Life Technologies). Specifically, 5μL of Lipofectamin 2000 and 0.6μg of HaloTag9-LaminB1 plasmid were diluted separated and incubated in OPTIMEM (Alfagene) for 30 min. The mixture was then added to confluent cells cultured and incubated for 6h in reduced serum medium (DMEM with 5% FBS). Cells were selected using 400μg/mL of G418 (Gibco, Life Technologies) for 14 days.

Drug treatments

To visualise DNA, cells were incubated for at least 1 hour with SiR-DNA (Spirochrome), at a final concentration of 10nM, for a maximum of 4 hours of imaging. To visualise HaloTag9 fluorescence, Janelia Fluor (JF) Ligand-646 (Promega) was added to the imaging media at a final concentration of 75nM. To affect cell rounding, a ROCK inhibitor (Y-27632) was used at 20μM (Sigma-Aldrich) and cells were incubated with the drug 30-

60 minutes prior to imaging. Calyculin-A (CalA, Abcam) was added to the cells during the imaging, at 20μM for RPE-1 cells and 50μM for U2-OS. To perturb microtubules, nocodazole (Noc, Sigma-Aldrich) was used at 3.3μM. Control cells were treated with the corresponding volume of DMSO (Sigma-Aldrich).

Transfections

Cells were transfected with the plasmid pRK5-Rap1[Q63E] plasmid (Rap1*; a gift from Jean de Gunzburg) for 48 hours as described before for plasmid transfections. Control cells were transfected with Lipofectamin 2000 (Invitrogen) only, in the same conditions. To deplete LaminA from RPE-1, cells were transfected with small interfering RNAs (siRNAs) using Lipofectamin RNAi Max (Life Technologies). Specifically, 5μL of Lipofectamin RNAi Max and 20nM of each siRNA were diluted separately, and then incubated in OPTIMEM (Alfagene) for 30 min. The mixture was then added to confluent cells cultured and incubated for 6h in reduced serum medium (DMEM with 5% FBS). Commercial ON-TARGETplus SMARTpool siRNAis (Dharmacon) were used. Commercial ON-TARGETplus SMARTpool nontargeting siRNAs and mock transfections were used as controls. Cells were analysed 72h after transfection and protein depletion efficiency verified by immunoblotting.

Plasmids

Plasmid	Type	Origin
pLKO.1 H2B-GFP	Lentiviral	Addgene
pRRL-mRFP-α-Tubulin	Lentiviral	In house
Rap1*	Transient Expression	Gift from Jean de Gunzburg
α-Tubulin-GFP	Lentiviral	In house
LBR-mCherry	Lentiviral	Gift from Stephen Royle
HaloTag9-LaminB1	Transient Expression	Gift from Tom Misteli
pLKO.1 shSUN1 - puro	Lentiviral	Sigma-Aldrich
pLKO.1 shSUN2 - puro	Lentiviral	Sigma-Aldrich
pinducer 20 DN-KASH	Lentiviral	Addgene #125554
pinducer 20 DN-KASHΔPPPL	Lentiviral	Addgene # 129280

Western Blotting

Cell extracts were collected after trypsinisation and centrifuged at 1200rpm for 5min, washed in Phosphate Buffered Saline (PBS) twice and resuspended in 30-50μL of lysis buffer (20nM HEPES/KOH, pH 7.9; 1mM EDTA pH8; 150mM NaCl; 0.5% NP40; 10% glycerol, 1:50 protease inhibitor; 1:100 Phenylmethylsulfonul fluoride). Cells were then flash frozen in liquid nitrogen and kept on ice for 30 min. DNA was pelleted after centrifugation at 14,000 rpm for 8min at 4ºC, the supernatant was collected, and protein concentration determined using the Bradford protein assay (Bio-Rad). Proteins were run on a 10% SDS-PAGE gel (30μg/lane) and transferred using a semi-dry blotting system

(Trans-Blot Turbo system, Bio-Rad) for 10 minutes at 25V, with constant amperage. Next, the membranes were blocked with 5% milk in PBS with 0.05% Tween-20 (PBS-T) for 1h, at room temperature (RT). The primary antibodies used were anti-LaminA (C-terminal; 1:1000; L1293; Sigma-Aldrich), anti-SUN1 (1:500; MABT892; Merck Millipore), anti-SUN2 (1:500; MABT880; Merck Millipore), anti-GAPDH (1:20000; 60004-1-Ig; Proteintech), anti-β-tubulin (1:5000; Ab6046; Abcam). All primary antibodies were incubated overnight at 4ºC with shaking. After three washes in PBS-T, the membranes were incubated with the secondary antibody for 1h, at RT. The secondary antibodies used were anti-mouse-HRP and anti-rabbit-HRP, at 1:5000. After three washes with PBS-T, the detection was performed with Clarity Western ECL Substrate (Bio-Rad). Acquisition of blots was performed with a Bio-Rad ChemiDoc XRS system using the IMAGE LAB software. Protein amount per sample was quantified using the same program, normalising the immunosignals to the loading control protein, GAPDH.

Immunofluorescence

Cells were seeded the day before the experiment in coverslips coated with fibronectin (25 µg/ml; F1141; Sigma-Aldrich; FBN). When necessary, cells were treated with the appropriate compounds, and fixed with 4% paraformaldehyde (PFA) in cytoskeleton buffer for 10 minutes at RT, and then extracted in PBS with 0.5% Triton-X100 (Sigma-Aldrich) for 5 minutes (or 30 minutes when using the antibody against Dynactin 1). Coverslips were then blocked using 10% FBS in 0.1% Triton-X100 for 30 minutes, at RT. These coverslips were afterwards incubated with the following primary antibodies: rabbit anti-SUN1 (1:200; HPA008346; Sigma-Aldrich), rabbit anti-SUN2 (1:200; HPA001209;

Sigma-Aldrich); mouse anti-Nesprin-2 (1:200; sc-398616; Santa Cruz Biotechnology), mouse α-tubulin (α-Tubulin B-5-1-2;1:1000; 32-2500; Sigma-Aldrich), rabbit β-tubulin (1:1000; Ab6046; Abcam); mouse anti-Lamin A+C (1:500; Ab8984; Abcam), rabbit anti-LaminB2 (1:1000; ab16048; Abcam), rabbit α-Dynactin 1 (1:200;PA5-21289; Invitrogen) in blocking solution. Primary antibody incubation was usually performed for 1 hour at RT, except when probing cells with the anti-Nesprin-2 and anti-Dynactin 1 antibodies, in which case incubation was completed overnight at 4ºC. Coverslips were washed with PBS-0.1%Tríton-X three times (5 minutes each) and incubated with the secondary antibodies (1:2000; Alexa-Fluor conjugated; Invitrogen), at RT for 1h. When appropriate, DAPI (1µg/mL; Invitrogen) was added to the secondary antibody mixture to stain DNA. Finally, coverslips were washed three times in PBS with 0.1% Triton-X100 and once in PBS, and sealed on a glass slide using mounting medium (20nM Tris pH 8, 0.5 N-propyl gallate, 90% glycerol). Images were acquired using an AxioImager Z1 (63x, Plan oil differential interface contract objective lens, 1.4NA; all from carl Zeiss) which is coupled to a CCD camera (ORCA-R2; Hamamatsu Photonics) using the Zen software (Carl Zeiss).

Micropatterning

Micropatterning was performed using a deep UV-light technique to normalise cell shape and adhesion area, as previously described[74]. Glass coverslips (square 22x22mm, 1.5, VWR; or round 25mm, 1.5, ThermoFisher) were activated with plasma (Zepto Plasma System, Diener Electronic) for 2 minutes. Following plasma treatment, coverslips were incubated with 0.2mg/mL PLL(20)-g[3,5]-PEG(2) (SuSoS) in 10 mM HEPES at pH 7.4, for 1 h, at RT. Coverslips were washed three times with water, and left to dry before being

placed on a synthetic quartz photomask (Delta Mask), previously activated with deep-UV light (PSD-UV, Novascan Technologies) for 5 min, using a 3uL of MilliQ water to seal it to the mask. The coverslips were then irradiated through the photomask with the UV lamp for 5 min and left to dry before being incubated with FBN (25 µg/ml; F1141; Sigma-Aldrich), in 100 mM NaHCO3 at pH 8.6, for 30 minutes, at RT. Whenever possible, 5 µg/ml Alexa 647–conjugated fibrinogen (ThermoFisher Scientific) was added to the fibronectin mix in order to visualise the pattern surfaces. Cells were added to the freshly incubated coverslips and allowed to spread for 15 minutes, before removing excess cells and new culture medium added, and cells left to fully adhere for another 12-16 hours.

Time lapse microscopy

Cells seeded in patterned or non-patterned surfaces are placed in Leibovitz´s-L15 medium (Life Technologies), supplemented with 10% FBS and Antibiotic-Antimycotic Solution 100X (AAS; Life Technologies) right before imaging, alongside the corresponding drugs, where indicated. Live cell imaging experiments were performed using temperature-controlled Nikon TE2000 microscopes equipped with a modified Yokogawa CSU-X1 spinning-disk head (Yokogawa Electric), an electro multiplying iXon+ DU-897 EM-CCD camera (Andor) and a filter wheel. Three laser lines were used to excite 488nm, 561nm and 647nm and all the experiments were done with immersion oil using a 60x 1.4NA Plan-Apo DIC (Nikon). Image acquisition was controlled by NIS Elements Ar software. Images were obtained with 17 z-stacks (0.5µm step) with a 20 second interval when assessing centrosome positioning during mitotic entry. For chromosome

segregation quantifications, images were obtained with 21 z-stacks (1μm step) with a 2-minute interval.

MATLAB custom algorithm for centrosome tracking

Analysis of centrosome positioning and behaviour during mitotic entry was performed using a custom-designed MATLAB (The MathWorks Inc, USA; v2018b) script[36] that contains a specialised workflow previously optimised for centrosome tracking, together with the reconstruction of both cellular and nuclear membranes in a 3D space. A pixel size of 0.176μm and a z-step of 0.5μm, were taken into consideration. Error correction methods were employed in cases where the standard automatic method was unable to correctly detect the two centrosomes and membranes. These correction methods involved, amongst others, manual centrosome position adjustment in all 3 coordinates (x, y and z) for each frame, and threshold correction for membrane reconstruction. From these membrane reconstructions, the algorithm was able to extract cell and nuclear major axis, as well as cell and nuclear membranes eccentricity and irregularity levels. From the coordinates obtained for centrosomes and with the nuclear and cell axis computed, the tool was able to calculate the angle between the two centrosomes that passed through the centroid of the nucleus (angle centrosome-centrosome) and the angle of the centrosomes axis relative to the long nuclear axis (angle centrosome-nucleus) for each frame/timepoint.

MATLAB custom algorithm for membrane fluorescence intensity measurement

Fluorescence signal quantification in the perinuclear area was done using a custom MATLAB script, as previously described[75]. In brief, five stacks corresponding to the middle section of the nucleus were sum-projected. The outline of the nuclear envelope is then manually selected, and a closed cubic spline curve is automatically generated to smoothly connect the points. The spline curve is then convolved with a disc-shaped kernel of variable diameter, which allows control of the ROI curve thickness. Fluorescence intensity is then calculated as the integrated signal inside the inner boundary of the defined ROI. All measurements were then normalised to the fluorescence intensity within the nucleus, as well as the ROI area.

Quantitative image analysis of Dynactin 1 levels

For the quantification of Dynactin 1 levels, images were analysed using ImageJ. A small region of interest (ROI) was defined at the nuclear envelope, and dynactin fluorescence intensity measured. A similar ROI was used to measure the levels of Dynactin 1 in the cytoplasm, and in a background region outside the cell. All fluorescence intensity values were then background corrected. This procedure was repeated three times in total for each cell, using different ROIs. The final values obtained for the background corrected fluorescence of both NE Dynactin 1 and Cytoplasmic Dynactin 1 were then averaged within the three measurements obtained.

Statistical analysis

At least three independent experiments were used for statistical analysis. Sample sizes and number or replicates are indicated in each figure legend. Normality of the samples was assessed using the Kolmogorov–Smirnov test. Statistical analysis for multiple group comparison was performed using a parametric one-way analysis of variance (ANOVA) when the samples had a normal distribution. Otherwise, multiple group comparison was done using a nonparametric ANOVA (Kruskal-Wallis). Multiple comparisons were analyzed using either post-hoc Student-Newman-Keuls (parametric) or Dunn's (nonparametric) tests. When comparing two experimental groups only, a parametric t test was used when the sample had a normal distribution, or a nonparametric Mann–Whitney test was used for samples without normal distribution. Comparison for multiple time-course datasets was done using an ANOVA Repeated Measures, when the samples had a normal distribution. Otherwise, group comparison was done using Repeated Measures ANOVA on Ranks. No power calculations were used. All statistical analyses were performed using the GraphPad Prism (Dotmatics). When comparing proportions between 2 populations, a z-score was calculated.

References

1. Antonin, W. & Neumann, H. Chromosome condensation and decondensation during mitosis. Curr. Opin. Cell Biol. **40**, 15–22 (2016).

2. Maddox, P. S., Portier, N., Desai, A. & Oegema, K. Molecular analysis of mitotic chromosome condensation using a quantitative time-resolved fluorescence microscopy assay. Proc. Natl. Acad. Sci. **103**, 15097–15102 (2006).

3. Dao, V. T., Dupuy, A. G., Gavet, O., Caron, E. & de Gunzburg, J. Dynamic changes in Rap1 activity are required for cell retraction and spreading during mitosis. J. Cell Sci. **122**, 2996–3004 (2009).

4. Mui, K. L., Chen, C. S. & Assoian, R. K. The mechanical regulation of integrin-cadherin crosstalk organizes cells, signaling and forces. J. Cell Sci. **129**, 1093–1100 (2016).

5. Zhai, Y., Kronebusch, P. J., Simon, P. M. & Borisy, G. G. Microtubule dynamics at the G2/M transition: abrupt breakdown of cytoplasmic microtubules at nuclear envelope breakdown and implications for spindle morphogenesis. J. Cell Biol. **135**, 201–214 (1996).

6. Mchedlishvili, N., Matthews, H. K., Corrigan, A. & Baum, B. Two-step interphase microtubule disassembly aids spindle morphogenesis. BMC Biol. **16**, 14 (2018).

7. Chugh, P. & Paluch, E. K. The actin cortex at a glance. J. Cell Sci. **131**, jcs186254 (2018).

8. Maddox, A. S. & Burridge, K. RhoA is required for cortical retraction and rigidity during mitotic cell rounding. J. Cell Biol. (2003). doi:10.1083/jcb.200207130

9. Linder, M. I. et al. Mitotic Disassembly of Nuclear Pore Complexes Involves CDK1- and PLK1-Mediated Phosphorylation of Key Interconnecting Nucleoporins. Dev. Cell **43**, 141-156.e7 (2017).

10. Heald, R. & McKeon, F. Mutations of phosphorylation sites in lamin A that prevent nuclear lamina disassembly in mitosis. Cell (1990). doi:10.1016/0092-8674(90)90470-Y

11. Jones, M. C., Askari, J. A., Humphries, J. D. & Humphries, M. J. Cell adhesion is regulated by CDK1 during the cell cycle. J. Cell Biol. **217**, 3203–3218 (2018).

12. Gavet, O. & Pines, J. Progressive Activation of CyclinB1-Cdk1 Coordinates Entry to Mitosis. Dev. Cell (2010). doi:10.1016/j.devcel.2010.02.013

13. Gheghiani, L., Loew, D., Lombard, B., Mansfeld, J. & Gavet, O. PLK1 Activation in Late G2 Sets Up Commitment to Mitosis. Cell Rep. (2017). doi:10.1016/j.celrep.2017.05.031

14. Toso, A. et al. Kinetochore-generated pushing forces separate centrosomes during bipolar spindle assembly. **184**, 365–372

15. Thompson, S. L. & Compton, D. A. Chromosome missegregation in human cells

arises through speci fi c types of kinetochore – microtubule attachment errors. **108**, 17974–17978 (2011).

16. Agircan, F. G., Schiebel, E. & Mardin, B. R. Separate to operate: control of centrosome positioning and separation. Philos. Trans. R. Soc. B Biol. Sci. **369**, 20130461–20130461 (2014).

17. Tanenbaum, M. E. & Medema, R. H. Mechanisms of Centrosome Separation and Bipolar Spindle Assembly. Dev. Cell **19**, 797–806 (2010).

18. van Heesbeen, R. G. H. P., Raaijmakers, J. A., Tanenbaum, M. E. & Medema, R. H. Nuclear envelope-associated dynein cooperates with Eg5 to drive prophase centrosome separation. Commun. Integr. Biol. **6**, (2013).

19. Raaijmakers, J. A. et al. Nuclear envelope-associated dynein drives prophase centrosome separation and enables Eg5-independent bipolar spindle formation. **31**, 4179–4190 (2012).

20. Kaseda, K., McAinsh, A. D. & Cross, R. A. Dual pathway spindle assembly increases both the speed and the fidelity of mitosis. Biol. Open **1**, 12–18 (2012).

21. Whitehead, C. M., Winkfein, R. J. & Rattner, J. B. The relationship of HsEg5 and the actin cytoskeleton to centrosome separation. Cell Motil. Cytoskeleton **35**, 298–308 (1996).

22. Silkworth, W. T., Nardi, I. K., Paul, R., Mogilner, A. & Cimini, D. Timing of centrosome separation is important for accurate chromosome segregation. **23**, 401–411 (2012).

23. Nunes, V. et al. Centrosome–nuclear axis repositioning drives the assembly of a bipolar spindle scaffold to ensure mitotic fidelity. Mol. Biol. Cell **31**, 1675–1690 (2020).

24. Petridou, N. I. & Skourides, P. A. FAK transduces extracellular forces that orient the mitotic spindle and control tissue morphogenesis. Nat. Commun. **5**, 5240 (2014).

25. Théry, M. et al. The extracellular matrix guides the orientation of the cell division axis. Nat. Cell Biol. **7**, 947–953 (2005).

26. Théry, M., Jiménez-Dalmaroni, A., Racine, V., Bornens, M. & Jülicher, F. Experimental and theoretical study of mitotic spindle orientation. Nature **447**, 493–496 (2007).

27. Guo, Y. & Zheng, Y. Lamins position the nuclear pores and centrosomes by modulating dynein. Mol. Biol. Cell **26**, 3379–3389 (2015).

28. Boudreau, V., Chen, R., Edwards, A., Sulaimain, M. & Maddox, P. S. PP2A-B55/SUR-6 collaborates with the nuclear lamina for centrosome separation during mitotic entry. Mol. Biol. Cell **30**, 876–886 (2019).

29. Lombardi, M. L. et al. The Interaction between Nesprins and Sun Proteins at the

Nuclear Envelope Is Critical for Force Transmission between the Nucleus and Cytoskeleton *. J. Biol. Chem. **286**, 26743–26753 (2011).

30. Zhang, X. et al. SUN1/2 and Syne/Nesprin-1/2 complexes connect centrosome to the nucleus during neurogenesis and neuronal migration in mice. Neuron **64**, (2009).

31. Malone, C. J. et al. The C. elegans Hook Protein, ZYG-12, Mediates the Essential Attachment between the Centrosome and Nucleus. Cell **115**, 825–836 (2003).

32. Splinter, D. et al. Bicaudal D2, Dynein, and Kinesin-1 Associate with Nuclear Pore Complexes and Regulate Centrosome and Nuclear Positioning during Mitotic Entry. PLOS Biol. **8**, e1000350 (2010).

33. Stiff, T. et al. Prophase-Specific Perinuclear Actin Coordinates Centrosome Separation and Positioning to Ensure Accurate Chromosome Segregation. Cell Rep. **31**, 107681 (2020).

34. Booth, A. J. et al. Contractile acto-myosin network on nuclear envelope remnants positions human chromosomes for mitosis. Elife **8**, (2019).

35. Théry, M. et al. The extracellular matrix guides the orientation of the cell division axis. **7**, (2005).

36. Castro, D., Nunes, V., Lima, J., Ferreira, J. & Aguiar, P. Trackosome: a computational toolbox to study the spatiotemporal dynamics of centrosomes, nuclear envelope and cellular membrane. (2020). doi:10.1101/2020.04.27.064204

37. Versaevel, M., Grevesse, T. & Gabriele, S. Spatial coordination between cell and nuclear shape within micropatterned endothelial cells. Nat. Commun. **3**, 671 (2012).

38. Kamranvar, S. A. et al. Integrin-Mediated Adhesion Promotes Centrosome Separation in Early Mitosis. Cells **11**, (2022).

39. Lancaster, O. M. et al. Mitotic Rounding Alters Cell Geometry to Ensure Efficient Bipolar Spindle Formation. Dev. Cell **25**, 270–283 (2013).

40. Sorce, B. et al. Mitotic cells contract actomyosin cortex and generate pressure to round against or escape epithelial confinement. Nat. Commun. **6**, 8872 (2015).

41. Dix, C. L. et al. The Role of Mitotic Cell-Substrate Adhesion Re-modeling in Animal Cell Division. Dev. Cell **45**, 132-145.e3 (2018).

42. Tachibana, K., Haghparast, S. M. A. & Miyake, J. Inhibition of cell adhesion by phosphorylated Ezrin/Radixin/Moesin. Cell Adh. Migr. **9**, 502–512 (2015).

43. Appelbaum, J., Blobel, G. & Georgatos, S. D. In vivo phosphorylation of the lamin B receptor. Binding of lamin B to its nuclear membrane receptor is affected by phosphorylation. J. Biol. Chem. **265**, 4181–4184 (1990).

44. Ma, Y. et al. Lamin B receptor plays a role in stimulating nuclear envelope production and targeting membrane vesicles to chromatin during nuclear envelope assembly through direct interaction with importin β. J. Cell Sci. **120**, 520 LP – 530

(2007).

45. Dantas, M., Oliveira, A., Aguiar, P., Maiato, H. & Ferreira, J. G. Nuclear tension controls mitotic entry by regulating cyclin B1 nuclear translocation. J. Cell Biol. **221**, e202205051 (2022).

46. Lombardi, M. L. & Lammerding, J. Keeping the LINC: The importance of nucleocytoskeletal coupling in intracellular force transmission and cellular function. in Biochemical Society Transactions (2011). doi:10.1042/BST20110686

47. Zhang, Q. et al. Mechanical Stabilization of the Glandular Acinus by Linker of Nucleoskeleton and Cytoskeleton Complex. Curr. Biol. **29**, 2826-2839.e4 (2019).

48. Gönczy, P., Pichler, S., Kirkham, M. & Hyman, A. A. Cytoplasmic Dynein Is Required for Distinct Aspects of Mtoc Positioning, Including Centrosome Separation, in the One Cell Stage Caenorhabditis elegans Embryo. J. Cell Biol. **147**, 135–150 (1999).

49. Robinson, J. T., Wojcik, E. J., Sanders, M. A., McGrail, M. & Hays, T. S. Cytoplasmic Dynein Is Required for the Nuclear Attachment and Migration of Centrosomes during Mitosis in Drosophila. J. Cell Biol. **146**, 597–608 (1999).

50. Bolhy, S. et al. A Nup133-dependent NPC-anchored network tethers centrosomes to the nuclear envelope in prophase. J. Cell Biol. **192**, 855–871 (2011).

51. Splinter, D. et al. BICD2, dynactin, and LIS1 cooperate in regulating dynein recruitment to cellular structures. Mol. Biol. Cell **23**, 4226–4241 (2012).

52. Belaadi, N. et al. SUN2 regulates mitotic duration in response to extracellular matrix rigidity. Proc. Natl. Acad. Sci. **119**, e2116167119 (2022).

53. May, C. K. & Carroll, C. W. Differential incorporation of SUN-domain proteins into LINC complexes is coupled to gene expression. PLoS One **13**, e0197621 (2018).

54. Kotak, S., Busso, C. & Gönczy, P. Cortical dynein is critical for proper spindle positioning in human cells. J. Cell Biol. **199**, 97–110 (2012).

55. Kiyomitsu, T. & Cheeseman, I. M. Chromosome- and spindle-pole-derived signals generate an intrinsic code for spindle position and orientation. Nat. Cell Biol. **14**, 311–317 (2012).

56. Taubenberger, A. V, Baum, B. & Matthews, H. K. The Mechanics of Mitotic Cell Rounding . Frontiers in Cell and Developmental Biology **8**, 687 (2020).

57. Tse, H. T. K., Weaver, W. M. & Di Carlo, D. Increased Asymmetric and Multi-Daughter Cell Division in Mechanically Confined Microenvironments. PLoS One **7**, e38986 (2012).

58. Matthews, H. K. et al. Changes in Ect2 Localization Couple Actomyosin-Dependent Cell Shape Changes to Mitotic Progression. Dev. Cell **23**, 371–383 (2012).

59. Fridolfsson, H. N. & Starr, D. A. Kinesin-1 and dynein at the nuclear envelope mediate the bidirectional migrations of nuclei. J. Cell Biol. **191**, 115–128 (2010).

60. Cadot, B. et al. Nuclear movement during myotube formation is microtubule and dynein dependent and is regulated by Cdc42, Par6 and Par3. EMBO Rep. **13**, 741–749 (2012).

61. Wilson, M. H. & Holzbaur, E. L. F. Opposing microtubule motors drive robust nuclear dynamics in developing muscle cells. J. Cell Sci. **125**, 4158–4169 (2012).

62. Magidson, V. et al. The Spatial Arrangement of Chromosomes during Prometaphase Facilitates Spindle Assembly. Cell **146**, 555–567 (2011).

63. Hu, D. J.-K. et al. Dynein Recruitment to Nuclear Pores Activates Apical Nuclear Migration and Mitotic Entry in Brain Progenitor Cells. Cell **154**, 1300–1313 (2013).

64. Baffet, A. D., Hu, D. J. & Vallee, R. B. Cdk1 Activates Pre-mitotic Nuclear Envelope Dynein Recruitment and Apical Nuclear Migration in Neural Stem Cells. Dev. Cell **33**, 703–716 (2015).

65. Gallisà-Suñé, N. et al. BICD2 phosphorylation regulates dynein function and centrosome separation in G2 and M. Nat. Commun. **14**, 2434 (2023).

66. Salina, D. et al. Cytoplasmic Dynein as a Facilitator of Nuclear Envelope Breakdown. Cell **108**, 97–107 (2002).

67. Beaudouin, J., Gerlich, D., Daigle, N., Eils, R. & Ellenberg, J. Nuclear Envelope Breakdown Proceeds by Microtubule-Induced Tearing of the Lamina. Cell **108**, 83–96 (2002).

68. Turgay, Y. et al. SUN proteins facilitate the removal of membranes from chromatin during nuclear envelope breakdown. J. Cell Biol. **204**, 1099–1109 (2014).

69. Silkworth, W. T. & Cimini, D. Transient defects of mitotic spindle geometry and chromosome segregation errors. 1–8 (2012).

70. Cimini, D., Moree, B., Canman, J. C. & Salmon, E. D. Merotelic kinetochore orientation occurs frequently during early mitosis in mammalian tissue cells and error correction is achieved by two different mechanisms. J. Cell Sci. **116**, 4213 LP – 4225 (2003).

71. Doherty, J. A. et al. ESR1/SYNE1 polymorphism and invasive epithelial ovarian cancer risk: an Ovarian Cancer Association Consortium study. Cancer Epidemiol. biomarkers Prev. a Publ. Am. Assoc. Cancer Res. cosponsored by Am. Soc. Prev. Oncol. **19**, 245–250 (2010).

72. Sjöblom, T. et al. The consensus coding sequences of human breast and colorectal cancers. Science **314**, 268–274 (2006).

73. Matsumoto, A. et al. Global loss of a nuclear lamina component, lamin A/C, and LINC complex components SUN1, SUN2, and nesprin-2 in breast cancer. Cancer Med. **4**, 1547–1557 (2015).

74. Azioune, A., Storch, M., Bornens, M. & Th, M. Simple and rapid process for single cell micro-patterning †. 1640–1642 (2009). doi:10.1039/b821581m

75. Ferreira, J. G., Pereira, A. J., Akhmanova, A. & Maiato, H. Aurora B spatially regulates EB3 phosphorylation to coordinate daughter cell adhesion with cytokinesis. J. Cell Biol. **201**, 709–724 (2013).